*Astronomy & Astrophysics* manuscript no. output
July 13, 2026


# Rotational excitation of singly and doubly deuterated formaldehyde induced by collisions with molecular hydrogen

## Rate coefficients and pressure broadening

Paul Pirlot Jankowiak[1], Takahiro Oyama[1], Alberto Macario[2], Chinmai Sai Jureddy[3], Alexandre Faure[4], Ian R. Sims[3,5], and Nami Sakai[1]

[1] Star and Planet Formation Laboratory, RIKEN Pioneering Research Institute (PRI), 2-1, Hirosawa, Wako, Saitama 351-0198, Japan
e-mail: paul.pirlotjankowiak@riken.jp,nami.sakai@riken.jp
[2] Université Sorbonne Paris Nord, Laboratoire de Physique des Lasers, CNRS, UMR 7538, F-93430 Villetaneuse, France

[3] Univ Rennes, CNRS, IPR (Institut de Physique de Rennes) - UMR 6251, F-35000 Rennes, France

[4] Univ Grenoble Alpes, CNRS, IPAG, 38000 Grenoble, France

[5] Institut universitaire de France (IUF), Paris, France

Received XXX; accepted YYY

**ABSTRACT**

This work presents calculations of state-to-state collisional rate coefficients for the rotational excitation of the deuterated formaldehyde isotopologs, HDCO and $D_2CO$, induced by collisions with molecular hydrogen, coupled with experimental verification by pressure-broadening measurements. Time-independent scattering calculations were performed using the close-coupling method to compute inelastic cross sections for collisions with both *para*-$H_2$ ($j_2 = 0$) and *ortho*-$H_2$ ($j_2 = 1$). These calculations are based on the $H_2CO$–$H_2$ potential energy surface previously determined at the CCSD(T) level of theory and transformed to account for the isotopic substitution. The resulting rate coefficients cover the lowest 100 rotational states of HDCO and 60 states of *ortho*- and *para*-$D_2CO$ with internal energies less than 200 $cm^{-1}$. Collisional data were obtained for temperatures up to 100 K for HDCO and $D_2CO$ and extended up to 300 K using the coupled-states approximation. The computed rate coefficients show systematic differences between *ortho*-$H_2$ and *para*-$H_2$ collisions, with the former generally yielding larger values by a factor of 2–3. Rate coefficients for HDCO–$H_2$ are found to be lower by a factor of 2 to 3 compared to those of $H_2CO$–$H_2$ and $D_2CO$–$H_2$. Pressure-broadening coefficients were also calculated using the random-phase approximation and compared with new laboratory measurements, yielding agreement by about 5–30%.

**Key words.** molecular data – molecular processes – radiative transfer – scattering – pressure broadening

## 1. Introduction

The abundance ratio between a deuterated molecule and its hydrogenated counterpart is often found to exceed the elemental D/H ratio by several orders of magnitude (Linsky et al. 2006), reaching values of several tens of percent in star-forming regions (Loinard et al. 2002) and, in some cases, approaching or exceeding unity, depending on the molecule (Caselli & Ceccarelli 2012; Ceccarelli et al. 2014; Nomura et al. 2022). Such extreme deuterium enhancement is a direct consequence of low-temperature fractionation chemistry. Differences in zero-point energies between deuterated and hydrogenated species drive exothermic reactions in the cold gas phase, resulting in the efficient incorporation of deuterium into molecules (Roueff et al. 2007). The degree of deuteration is therefore highly sensitive to temperature and density, providing a robust diagnostic of physical conditions (Ceccarelli et al. 2007). Furthermore, since deuterium enrichment proceeds with different efficiencies in gas-phase reactions and on grain surfaces, deuteration levels offer key insights into molecular formation pathways (Podio et al. 2024).

Formaldehyde ($H_2CO$) plays a central role in astrochemistry as a key intermediate in the grain-surface formation of methanol ($CH_3OH$), the most abundant complex organic molecule in the interstellar medium (ISM) (Ceccarelli et al. 2023; Sabatini et al. 2024). It is also an important precursor to more complex organic molecules and is closely linked to prebiotic chemistry, including pathways leading to amino acids that may ultimately be delivered to planetary systems (Öberg 2016; Drozdovskaya et al. 2019). Formaldehyde and its deuterated isotopologs (HDCO and $D_2CO$) form efficiently in cold environments characterized by CO depletion, such as pre-stellar and starless cores (Bacmann et al. 2003; Miettinen et al. 2012; Li et al. 2022; Redaelli et al. 2025; Spezzano et al. 2025). These species have also been widely detected in low-mass protostars and hot corinos (Persson et al. 2018; Okoda et al. 2020; Evans et al. 2023; Chahine et al. 2024; Mercimek et al. 2025), as well as in planet-forming disks (Podio et al. 2024). Therefore, they provide valuable probes of the physical conditions and chemical history of star-forming regions (Evans et al. 2023; Chahine et al. 2024).
In star-forming regions, the gas density is often insufficient for local thermodynamic equilibrium (LTE) to be valid for molec-



Article published by EDP Sciences, to be cited as https://doi.org/10.1051/0004-6361/202660504

ular excitation (Tonolo 2025), although LTE conditions may be approached in dense regions such as protostellar disks. Therefore, molecular abundances and excitation conditions must be inferred using radiative transfer modeling that accounts for the competition between radiative and collisional processes. In this context, accurate state-to-state inelastic rate coefficients for collisions between formaldehyde isotopologs and molecular hydrogen – the dominant interstellar collider – are essential.

Collisional excitation of $H_2CO$ by interstellar partners has been the subject of several previous studies. The first extensive set of collisional rate coefficients for $H_2CO$–He collisions was reported by Green (1991), based on quantum close-coupling (CC) calculations up to 20 K and extended to 300 K using the coupled-states (CS) approximation (McGuire 1975). The corresponding interaction potential was derived within the rigid rotor approximation at the Hartree–Fock level (Garrison et al. 1975). More recently, Troscompt et al. (2009) computed a high-quality potential energy surface (PES) for the $H_2CO$–$H_2$ system at the coupled cluster level of theory (Pople et al. 1987). Using this PES, Wiesenfeld & Faure (2013) performed quantum inelastic scattering calculations for collisions of $H_2CO$ with *ortho*- and *para*-$H_2$, employing CC and CS methods up to 300 K for the 40 lowest rotational levels of *ortho*- and *para*-$H_2CO$. Dedicated CC calculations also showed good agreement with experimental pressure-broadening measurements at temperatures below 25 K (Mengel & De Lucia 2000). In contrast, Wiesenfeld & Faure (2013) found large discrepancies when comparing $H_2$-based rate coefficients with those obtained by scaling He data, showing that helium is a bad proxy for molecular hydrogen in collisions with $H_2CO$. Very recently, Santelices Rosas et al. (2026) reported the first collisional data for formaldehyde-deuterated isotopologs in interaction with He, based on ab initio PESs for the $H_2CO$–He and HDCO–He complexes, and confirmed the inadequacy of the mass-scaling relation for these collisional systems.

In this work, we investigated the collisional excitation of the singly and doubly deuterated formaldehyde isotopologs, HDCO and $D_2CO$, induced by molecular hydrogen, with the aim of enabling accurate non-LTE modeling of their interstellar emission lines. State-to-state rate coefficients for the HDCO–$H_2$ and $D_2CO$–$H_2$ systems were computed using the $H_2CO$–$H_2$ PES developed by Troscompt et al. (2009), from which the interaction potentials for the deuterated species were derived. The reliability of the resulting PESs was further assessed by comparing theoretical pressure-broadening coefficients with laboratory measurements performed using the SUMIRE (Spectrometer Using superconductor MIxer Receiver; Watanabe et al. (2021)) apparatus.

The paper is organized as follows. Section 2 describes the theoretical framework used to compute cross sections and rate coefficients for HDCO–$H_2$ and $D_2CO$–$H_2$, as well as for pressure-broadening calculations. Section 3 presents comparisons of the cross sections, rate coefficients, and pressure-broadening coefficients. In Sect. 4, we illustrate the astrophysical implications of the new collisional data through a simple radiative transfer application. Finally, Sect. 5 summarizes the main results of this study.

## 2. Methods

### 2.1. Potential energy surfaces

The PES for the $H_2CO$–$H_2$ system was computed by Troscompt et al. (2009) at the CCSD(T) level of theory using a complete basis set extrapolation scheme (Pople et al. 1987; Jankowski & Szalewicz 2005). Both molecules were treated as rigid rotors fixed at their ground-state, vibrationally averaged geometries. For $H_2CO$, the adopted structural parameters are $r_{CH}$ = 1.1171 Å, $r_{CO}$ = 1.2072 Å, and $\widehat{HCH}$ = 116°14′ (Johnson et al. 1972; Duncan 1974), while the $H_2$ bond length was set to $r_{HH}$ = 1.449 Å (Faure et al. 2005).

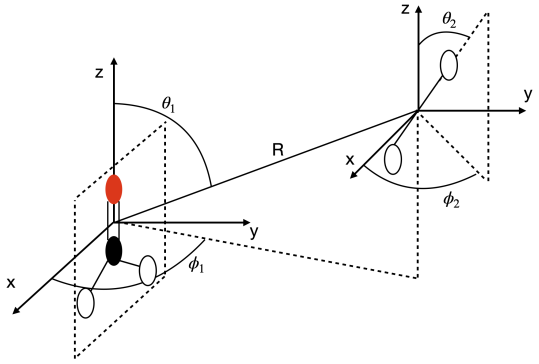


**Fig. 1.** Body-fixed coordinate system used to describe the $H_2CO$–$H_2$ complex. The $H_2CO$ molecule lies in the $x$–$z$ plane.

The body-fixed coordinate system used to describe the $H_2CO$–$H_2$ complex is shown in Fig. 1. The Jacobi vector **R** connects the centers of mass of the two molecules. The angles $(\theta_1, \phi_1)$ define the orientation of the $H_2$ center of mass with respect to the $H_2CO$ frame, while $(\theta_2, \phi_2)$ describe the orientation of the $H_2$ internuclear axis. The $C_{2v}$ symmetry axis of $H_2CO$ coincides with the body-fixed $z$-axis, and the molecule lies in the $x$–$z$ plane. The global minimum of the PES is found to be $D_e$ = 321 cm$^{-1}$ at $R$ = 5.6 $a_0$, with $(\theta_1, \phi_1)$ = (80°, 0°) and $(\theta_2, \phi_2)$ = (118°, 0°) (Troscompt et al. 2009).

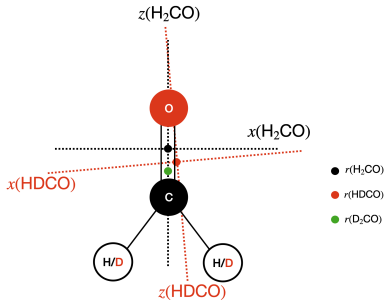


**Fig. 2.** Inertial axes of the $H_2CO$ and HDCO molecules. The shifts in the centers of mass have been exaggerated.

The isotopic substitution of hydrogen by deuterium modifies the position of the molecular center of mass while leaving the PES invariant within the Born–Oppenheimer approximation. To evaluate the interaction energy for a given geometry of the HDCO–$H_2$ complex defined by the coordinates $(R', \theta'_1, \phi'_1, \theta'_2, \phi'_2)$, the corresponding Cartesian coordinates $(x', y', z')$, denoting the coordinates of the center of mass of $H_2$ with respect to the HDCO frame, were first determined following

$$x' = R' \sin(\theta'_1) \cos(\phi'_1), \quad (1)$$
$$y' = R' \sin(\theta'_1) \sin(\phi'_1), \quad (2)$$
$$z' = R' \cos(\theta'_1). \quad (3)$$

The transformation from the HDCO–$H_2$ to $H_2CO$–$H_2$ frame **r'** = $(x', y', z') \rightarrow$ **r** = $(x, y, z)$ was then obtained by applying

a translation to account for the shift in the center of mass and a rotation of the inertia axes:

$$\mathbf{r} = \mathcal{R} \cdot \mathbf{r'} + \boldsymbol{\delta}_{\rm com}, \tag{4}$$

with $\boldsymbol{\delta}_{\rm com} = (\delta_x, 0, \delta_z)$ being the coordinates of the displaced center of mass and $\mathcal{R}$ the rotation matrix about the $y$-axis by the angle $\gamma$ (see Fig. 2).

Subsequently, the Jacobi coordinates $(R, \theta_1, \phi_1)$ in the $H_2CO$–$H_2$ frame were derived as

$$R = \sqrt{x^2 + y^2 + z^2}, \tag{5}$$

$$\theta_1 = \arctan\left(\frac{\sqrt{x^2 + y^2}}{z}\right), \tag{6}$$

$$\phi_1 = \arctan\left(\frac{y}{x}\right). \tag{7}$$

The Cartesian coordinates $\mathbf{r_H'} = (x'_H, y'_H, z'_H)$ defining the position of one of the H atoms of the $H_2$ bond, constructed similarly to Eqs. 1–3, are also affected by the shift and follow the same transformation rules given by Eqs. 4, 6, and 7. Figure 2 illustrates the displacement of the center of mass and the corresponding inertia axes for the deuterated isotopologs. For a single deuteration of $H_2CO$, the center of mass is displaced by $\delta_x$ = 0.0582 $a_0$, $\delta_z$ = –0.0732 $a_0$ , and the rotation angle about the $y$-axis (passive rotation) is $\gamma$ = +5.306°. In the case of double deuteration, the coordinates for the $D_2CO$–$H_2$ system are defined as $(R'', \theta''_1, \phi''_1, \theta''_2, \phi''_2)$ and follow the same procedure as for HDCO–$H_2$, where the center of mass shifts by $\delta_z = -0.1418\ a_0$ along the $z$-axis and $\gamma = 0°$.

The solution to the CC equations relies on the analytical description of the PES. The interaction potential for the HDCO–$H_2$ system, $V(R', \theta'_1, \phi'_1, \theta'_2, \phi'_2)$, can be expanded over spherical harmonics following (Valiron et al. 2008)

$$V(R', \theta'_1, \phi'_1, \theta'_2, \phi'_2) = \sum_{l_1 m_1 l_2 l} v_{l_1 m_1 l_2 l}(R')\, \bar{t}_{l_1 m_1 l_2 l}(\theta'_1, \phi'_1, \theta'_2, \phi'_2), \tag{8}$$

where $v_{l_1 m_1 l_2 l}(R')$ represents the radial expansion coefficient. The tensor ranks $l_1$, $l_2$ correspond to the orientations of HDCO and $H_2$, and $l$ the tensor rank of the collision vector orientation satisfies the relation $|l_1 - l_2| < l < l_1 + l_2$. The angular functions $\bar{t}_{l_1 m_1 l_2 l}$ are defined as

$$\begin{aligned} \bar{t}_{l_1 m_1 l_2 l} &= \alpha_{l_1 m_1 l_2 l}(1 + \delta_{m_1 0})^{-1} \\ &\times \sum_{r_1 r_2} \begin{pmatrix} l_1 & l_2 & l \\ r_1 & r_2 & r \end{pmatrix} Y_{l_2 r_2}(\theta'_2, \phi'_2) Y_{l r}(\theta'_1, \phi'_1) \\ &\times [\delta_{m_1 r_1} + (-1)^{l_1 + m_1 + l_2 + l} \delta_{-m_1 r_1}], \end{aligned} \tag{9}$$

with the normalization factor

$$\alpha_{l_1 m_1 l_2 l} = \left[2(1 + \delta_{m_1 0})^{-1}(2l_1 + 1)^{-1}\right]^{-1/2}. \tag{10}$$

Here, $(\cdots)$ denotes a Wigner 3$j$ symbol, and the values $m_1, r_i$ satisfy the relations $m_1 \leq l_1$ and $-l_i \leq r_i \leq l_i$. Owing to the homonuclear nature of $H_2$, only even values of $l_2$ contribute to the expansion of the interaction potential. Also, the break in $C_{2v}$ symmetry involves both odd and even $m_1$ values. The radial coefficients ($v_{l_1 m_1 l_2 l}(R')$) were obtained by fitting the HDCO–$H_2$ PES using a linear least-squares procedure over Eq. 8. The fit was performed for intermolecular separations between 4 and 15 $a_0$ using a uniform random sample of 3000 angular configurations. All statistically significant terms $v_{l_1 m_1 l_2 l}$ were selected iteratively using the procedure described in Valiron et al. (2008). The final expansion includes anisotropies up to $l_1$ = 11 for HDCO and $l_2$ = 4 for $H_2$, resulting in 193 $\bar{t}_{l_1 m_1 l_2 l}$ functions. The root-mean-square (rms) error of the fit is found to be better than 5 cm$^{-1}$ for $R > 5.5\ a_0$, including the region of the global minimum, and better than 1 cm$^{-1}$ for $R > 6.5\ a_0$. This is similar to the rms error of the reference $H_2CO$–$H_2$ PES, indicating that no appreciable fitting errors were introduced despite breaking the $C_{2v}$ symmetry. Cubic spline interpolation was finally employed over the whole intermolecular distance range and was smoothly connected with standard extrapolations (power laws) to provide continuous radial expansion coefficients suitable for scattering calculations. Full details can be found in (Valiron et al. 2008).

The interaction potential for the $D_2CO$–$H_2$ system, $V(R'', \theta''_1, \phi''_1, \theta''_2, \phi''_2)$, was fitted similarly to that of the HDCO–$H_2$ PES. Following Troscompt et al. (2009) for the $H_2CO$–$H_2$ PES, the expansion was truncated at $l_{1,\rm max}$ = 13 and $l_{2,\rm max}$ = 4, yielding 146 expansion coefficients. This resulted in a rms error better than 1 cm$^{-1}$ for $R > 5.5\ a_0$, including the region of the global minimum, and better than 0.1 cm$^{-1}$ for $R > 6.5\ a_0$. The rms error of the $D_2CO$–$H_2$ PES is thus much better than the reference $H_2CO$–$H_2$ PES. This is expected since the symmetry remains unchanged and the same 146-term angular expansion was adopted.

Figure 3 compares the contour plots of the interaction potential for the $H_2CO$–$H_2$, HDCO–$H_2$, and $D_2CO$–$H_2$ systems at $R$ = 5.62 $a_0$, close to the equilibrium separation. The overall similarity of the surfaces reflects the small displacement of the center of mass induced by isotopic substitution. Noticeable differences are attributed in the repulsive region of the interaction energy.

### 2.2. Scattering calculations

Quantum time-independent scattering calculations were performed using the MOLSCAT program (Hutson & Le Sueur 2019), which treats collisions between an asymmetric top and a linear rotor. Table 1 summarizes the spectroscopic constants used in our scattering calculations to describe the rotational levels of HDCO and $D_2CO$. These are labeled by the values $j_{k_a k_c}$, where $j$ is the total rotational angular momentum and $k_a$ and $k_c$ are its projections along the principal inertia axes. For molecular hydrogen, the rotational constant $B$ = 59.322 cm$^{-1}$ was adopted (Huber & Herzberg 1979). The reduced mass used for the HDCO–$H_2$ and $D_2CO$–$H_2$ collisional systems are $\mu$ = 1.892655 u and 1.896344 u, respectively.

Because $D_2CO$ contains two identical deuterium nuclei, nuclear spin statistics leads to two distinct species *ortho*-$D_2CO$ (even $k_a$) and *para*-$D_2CO$ (odd $k_a$). A similar separation applies to the $H_2$ collider, which exists as *ortho*-$H_2$ and *para*-$H_2$ for odd and even values of the rotational quantum number $j_2$, respectively.

State-to-state inelastic cross sections for HDCO and $D_2CO$ in collision with *para*-$H_2$ ($j_2 = 0$) and *ortho*-$H_2$ ($j_2 = 1$) were computed using the CC method. For collisions with *para*-$H_2$, CC calculations were carried out up to a total energy of 1100 cm$^{-1}$. For *ortho*-$H_2$ collisions, CC calculations were feasible up to 518.7–718.7 cm$^{-1}$, depending on the isotopolog, and were ex-

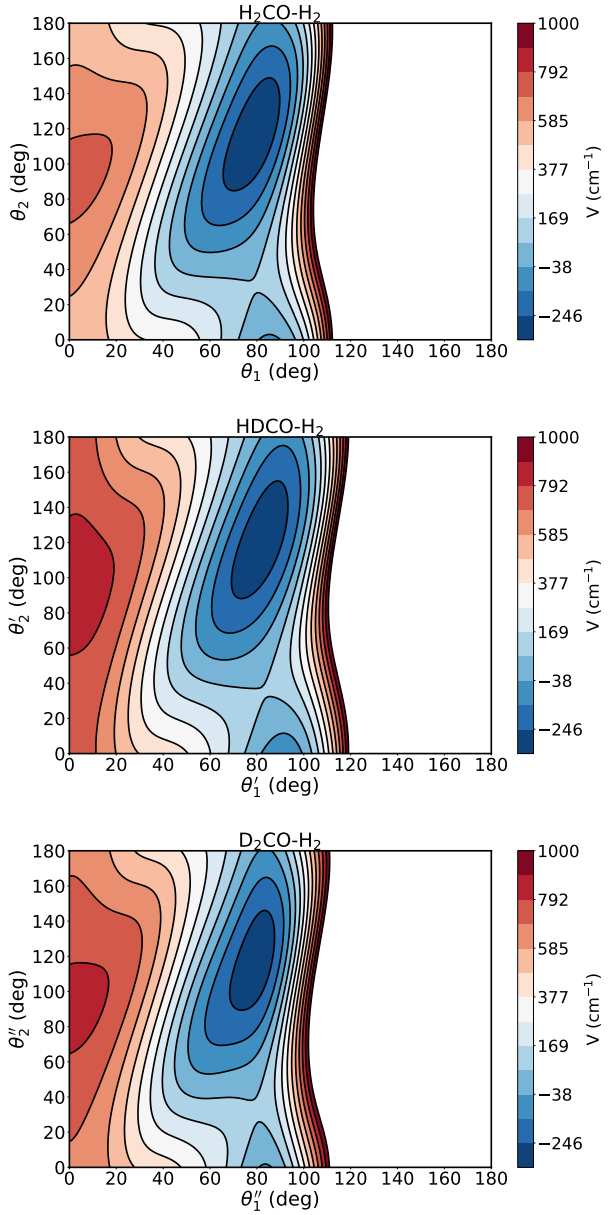


**Fig. 3.** Contour plots of the interaction potential for the $H_2CO$–$H_2$, HDCO–$H_2$, and $D_2CO$–$H_2$ complexes at $R = 5.62\ a_0$, $\phi_1 = 0°$, and $\phi_2 = 0°$, corresponding to the geometry of the global minimum of the $H_2CO$–$H_2$ PES.

**Table 1.** Spectroscopic parameters used in our scattering calculations.

| Parameter | HDCO | $D_2CO$ |
|---|---|---|
| $A$ | 6.6083047 | 4.7250681 |
| $B$ | 1.1645003 | 1.0768314 |
| $C$ | 0.98605116 | 0.8734849 |
| $D_j$ | $2.06\times10^{-6}$ | $1.53\times10^{-6}$ |
| $D_{jk}$ | $2.37\times10^{-5}$ | $2.21\times10^{-5}$ |
| $D_k$ | $2.008\times10^{-4}$ | $1.484\times10^{-4}$ |

**Notes.** Rotational constants $(A, B, C)$ and quartic centrifugal distortion constants $(D_j, D_{jk}, D_k)$ are in wave numbers and taken from Zakharenko et al. (2015).

tended to ~1200 $cm^{-1}$ using the CS approximation (McGuire 1975) due to the high computational cost.

Integral cross sections were computed for transitions among the lowest 100 rotational levels of HDCO and the lowest 60 levels of *ortho*-$D_2CO$ and *para*-$D_2CO$, corresponding to internal energies up to ~200 $cm^{-1}$. Convergence was checked with respect to the number of partial waves and the size of the rotational basis. For collisions with *para*-$H_2$, the $H_2$ rotational basis included $j_2 = (0, 2)$ up to total energies of 300–400 $cm^{-1}$, depending on the isotopolog, and was restricted to $j_2 = 0$ at higher energies up to ~1100 $cm^{-1}$. For *ortho*-$H_2$ collisions, the scattering basis was limited to $j_2 = 1$ over the full energy range. Further details on convergence tests and on the comparison between CC and CS calculations are provided in Appendices A and B.

State-to-state rate coefficients for transitions in HDCO–$H_2$ and $D_2CO$–$H_2$ collisions were determined from the computed inelastic cross sections $\sigma_{i\to f}(E_c)$. Rate coefficients based on CC cross sections were obtained over the temperature range 5–100 K for HDCO–$H_2$ and $D_2CO$–$H_2$. An additional set of rate coefficients up to 300 K was computed using CS cross sections. In all cases, rate coefficients were calculated according to

$$k_{i\to f}(T) = \left(\frac{8}{\pi\mu(k_B T)^3}\right)^{1/2} \times \int_0^\infty \sigma_{i\to f}(E_c)\, E_c\, e^{-E_c/k_B T}\, dE_c, \quad (11)$$

where $\mu$ is the reduced mass of the collisional system, $k_B$ is the Boltzmann constant, and $E_c$ is the collision energy.

### 2.3. Pressure-broadening calculations

The reliability of the HDCO–$H_2$ and $D_2CO$–$H_2$ PESs can be assessed by computing pressure-broadening coefficients and comparing them with laboratory measurements at room temperature. In principle, the calculation of pressure-broadening cross sections within the CC framework requires the accurate convergence of both inelastic and elastic contributions, as both processes contribute to collisional line broadening (Ball & De Lucia 1998). However, the convergence of elastic cross sections becomes particularly demanding at high temperatures, where large angular momentum expansions are required, resulting in substantial computational costs.

In this work, pressure-broadening calculations were performed using the random-phase approximation (RPA; Faure et al. (2013)). Within this approach, the differential elastic scattering amplitudes are neglected, and the pressure-broadening cross section $\sigma^{PB}_{i\to f}(T)$ is expressed solely as a sum over inelastic contributions. Subsequently, the pressure-broadening parameter $\gamma_{i\to f}(T)$ is computed as

$$\gamma_{i\to f}(T) = 2.236 \frac{\sigma^{PB}_{i\to f}(T)}{\sqrt{\mu T}}, \quad (12)$$

where $\sigma^{PB}_{i\to f}(T)$ is expressed in square angstroms and determined assuming a statistical distribution of $H_2$ at room temperature (see Faure et al. (2013) for the detailed formalism) and $\gamma_{i\to f}(T)$ is expressed in megahertz per torr. This approximation significantly reduces the computational effort, as it relies only on the set of inelastic cross sections or rate coefficients already obtained from scattering calculations.

A known limitation of the RPA is its reduced validity at low temperatures, i.e., below ~200 K for typical van der Waals sys-

tems, where elastic scattering dominates the line broadening process. At higher temperatures, however, the relative contribution of inelastic collisions increases, and the RPA is expected to be reliable. For the present study, which focuses on comparisons at room temperature, the impact of this approximation is therefore expected to be minor.

## 3. Results

In the following, collisional cross sections and rate coefficients are discussed for the data computed with the CC method, except when explicitly formulated. Discussions about differences between CC and CS approaches can be found in Appendix B.

### 3.1. Cross sections and rate coefficients

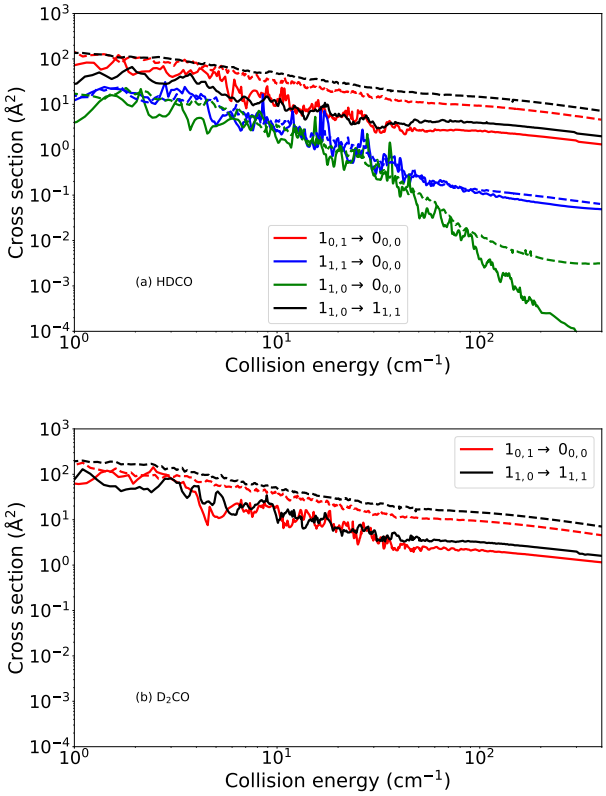


**Fig. 4.** De-excitation cross sections for several $j_{k_a k_c} \rightarrow j'_{k'_a k'_c}$ transitions of (a) HDCO and (b) $D_2CO$ as a function of the collision energy. The solid lines represent *para*-$H_2$ collisions, while the dashed lines represent *ortho*-$H_2$ collisions.

Figure 4 shows the collision energy dependence of the rotational de-excitation cross sections from the $j = 1$ energy level for HDCO and $D_2CO$ collisions induced by *para*-$H_2$ ($j_2 = 0$) and *ortho*-$H_2$ ($j_2 = 1$). For most transitions, the *ortho*-$H_2$ cross sections are larger than the *para*-$H_2$ ones, as the quadrupole moment of $H_2$ ($j_2 > 0$) involves more anisotropies of the potential compared to $H_2$ in the ground rotational state ($j_2 = 0$). We can notice the presence of resonant features in the low energy regime, which can be attributed to the formation of quasi-bound states in the potential well. The shape of these resonances look less pronounced for the *ortho*-$H_2$ collisions due to their large number and overlap.

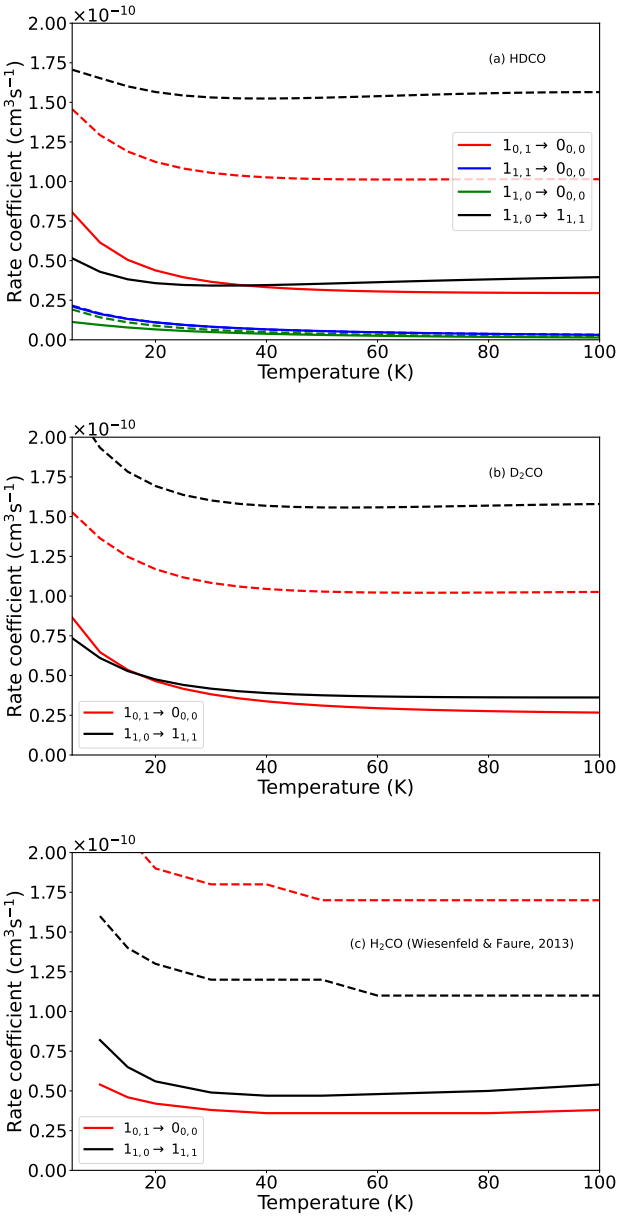


**Fig. 5.** Temperature dependence of several rate coefficients for (a) HDCO, (b) $D_2CO$ and (c) $H_2CO$ (taken from Wiesenfeld & Faure (2013)). The solid lines represent *para*-$H_2$ collisions, while the dashed lines represent *ortho*-$H_2$ collisions.

The same differences and tendencies are reported in Fig. 5 for the rate coefficients, where we also include $H_2CO$–$H_2$ data from Wiesenfeld & Faure (2013). In the present work, state-to-state rate coefficients generally differ by up to a factor of 2–3 between the two colliders, highlighting the importance of treating both *ortho*- and *para*-$H_2$ as separate species. This trend is also observed in many studies involving the collisions of neutral species with molecular hydrogen (e.g., Schewe et al. (2015); Dagdigian (2022b); Pirlot Jankowiak et al. (2024)). On the other hand, we note that the rate coefficients for HDCO–$H_2$ transitions generally have a lower magnitude than those for $H_2CO$–$H_2$ and $D_2CO$–$H_2$, regardless of the collider. Also, collisions involving $H_2CO$ and $D_2CO$ seem to yield rate coefficients of similar magnitude.

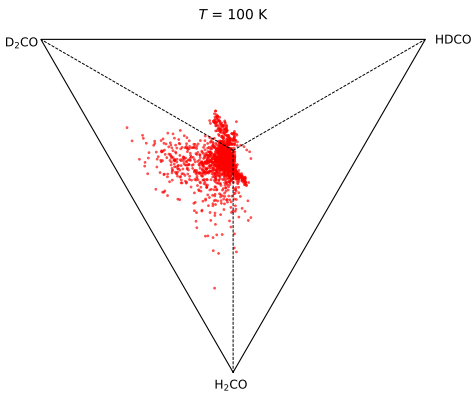


**Fig. 6.** Dalitz plot comparing the rate coefficients for $H_2CO$, HDCO, and $D_2CO$ in collision with *para*-$H_2$($j_2 = 0$) at $T = 100$ K.

A qualitative comparison between collisions of $H_2CO$, HDCO, and $D_2CO$ isotopologs can be made with a Dalitz plot (Babikov et al. 2002; Joy et al. 2024), as displayed in Fig. 6 where collisions include the *para*-$H_2$ collider. Similar results were found for collisions with *ortho*-$H_2$ but are not shown here. In this plot, the rate coefficients $k_{H_2CO}$, $k_{HDCO}$, and $k_{D_2CO}$ have been normalized as

$$\bar{k}_{H_2CO} = \frac{k_{H_2CO}}{k_{H_2CO} + k_{HDCO} + k_{D_2CO}}, \quad (13)$$

$$\bar{k}_{HDCO} = \frac{k_{HDCO}}{k_{H_2CO} + k_{HDCO} + k_{D_2CO}}, \quad (14)$$

$$\bar{k}_{D_2CO} = \frac{k_{D_2CO}}{k_{H_2CO} + k_{HDCO} + k_{D_2CO}}, \quad (15)$$

and satisfy the relation $\bar{k}_{H_2CO} + \bar{k}_{HDCO} + \bar{k}_{D_2CO} = 1$ within a triangular area. Each point represents a transition and can be interpreted as follows: if a point lies at the center of the triangle, the rate coefficient for the three isotopologs is the same. If a point lies on one of the diagonals, the rate coefficient for the isotopolog corresponding to that diagonal differs from the other two, which are similar. In particular, if the point is closer to the edge of the triangle, the rate coefficient for the isotopolog of the diagonal is larger than the others, whereas the opposite is true if the point is farther from the edge but still on the diagonal. Thus, the rate coefficients for the HDCO molecule are globally lower than those for the two other colliders by a factor of 2 to 3, as evidenced by the clustering of points below and near the HDCO diagonal, reflecting $k_{HDCO} < k_{D_2CO} \sim k_{H_2CO}$. Moreover, the point distribution suggests larger rate coefficients for the $H_2CO$ collisions than for the $D_2CO$ collisions. Most of the transitions deviate by a factor of 2. Since isotopic substitution has a minor impact on the PES of $D_2CO$–$H_2$, these magnitude differences in rate coefficients are mainly attributed to the differences between the spectroscopic constants of $H_2CO$ and $D_2CO$. However, the isotopic substitution for HDCO is significant due to the breaking of $C_{2v}$ symmetry, which allows additional transitions. This results in lower rate coefficients for HDCO.

Figure 7 displays the distribution of all available rate coefficients for the $\Delta k_a = 0,1,2$ transitions in the case of HDCO and $D_2CO$ in collision with $H_2$. The propensity rules observed for the $D_2CO$–$H_2$ rate coefficients are the same as for the $H_2CO$–$H_2$ transitions and are not shown here. One can clearly see a propensity rule for the $\Delta k_a = 0$ transitions, regardless of the collider. These can be explained by the conservation of the projection of the angular momentum along the $a-$axis (the axis of the smallest moment of inertia). Of course, not all transitions follow this trend as the interaction potential also impacts the scattering process. It is worth noting that even though such a rule is often observed in collisions involving asymmetric tops (Faure et al. 2011; Ben Khalifa & Loreau 2024; Sogomonyan et al. 2025), several studies have shown that this tendency is not universal for this type of system (Demes et al. 2024, 2025). We can also see additional transitions in $\Delta k_a = 1$ for collisions involving HDCO due to the break in molecular symmetry when applying a single deuteration of $H_2CO$. These transitions can be lower than those for $D_2CO$–$H_2$ by up to two orders of magnitude, highlighting the importance of explicit calculations for HDCO interactions with $H_2$ , which cannot be predicted by scaling relations using $H_2CO$–$H_2$ or $D_2CO$–$H_2$ data. This result has been observed in other collisional studies for asymmetric tops involving isotopic substitution, such as for $H_2O$ (Wiesenfeld et al. 2011) or $H_2S$ (Dagdigian 2022a). Finally, we do not observe a clear trend for the $\Delta j$ or $\Delta k_c$ transitions.

### 3.2. Pressure broadening

Figure 8 summarizes the experimental pressure-broadening parameters $\gamma_{i\to f}(T)$ measured at room temperature for several transitions of $H_2CO$ isotopologs in collision with *normal*-$H_2$ using the Spectrometer Using superconductor MIxer Receiver (SUMIRE; Watanabe et al. (2021)) setup, together with the corresponding theoretical values obtained in this work. The details of the experiments are described in Appendix C. The theoretical and experimental values agree well on an absolute scale to within ∼30%, with some systematic trends observable.

For the $H_2CO$–$H_2$ system, the theoretical pressure-broadening coefficients systematically underestimate the experimental measurements, whereas for the HDCO–$H_2$ and $D_2CO$–$H_2$ systems the calculated values slightly overestimate the experimental ones. At 295 K, the equilibrium ortho-to-para ratio of $H_2$ is 3, and both *ortho*-$H_2$ and *para*-$H_2$ contribute significantly to pressure broadening. We note that at this temperature, inelastic CC calculations contributing at high collision energies were performed using a restricted rotational basis limited to $j_2 = 0$ for *para*-$H_2$ (see Appendix B for details about the differences in rotational basis). In addition, calculations involving *ortho*-$H_2$ were carried out using the CS approximation for all isotopologs. For both HDCO and $D_2CO$ in collision with $H_2$, the agreement between CS and CC calculations are, nonetheless, reasonable. The reliability of the RPA used for pressure broadening is difficult to quantify precisely due to the lack of fully converged elastic cross sections. Nevertheless, the $D_2CO$–$H_2$ pressure-broadening coefficients are expected to deviate from experiment by no more than about 30% at room temperature, in line with previous findings for the $H_2O$–$H_2$ system (Faure et al. 2013).

For the $H_2CO$–$H_2$ system, we also included the collisional data from Wiesenfeld & Faure (2013), who employed the CS method at total energies above 330 $cm^{-1}$ for both *ortho*-$H_2$ and *para*-$H_2$ collisions, using a rotational basis $j_2 = 1$ and $j_2 = 0$, respectively. In that work, deviations between CS calculations with $j_2 = (0, 2)$ and $j_2 = 0$ were found to decrease with increasing collision energy. However, it remains unclear whether CS calculations systematically underestimate CC results, which could partly account for (along with the rotational basis sets) the lower theoretical pressure-broadening coefficients obtained for $H_2CO$ compared to experiment. This would suggest a refinement of these calculations at high temperatures. Overall, the agreement between the theoretical and experimental pressure-

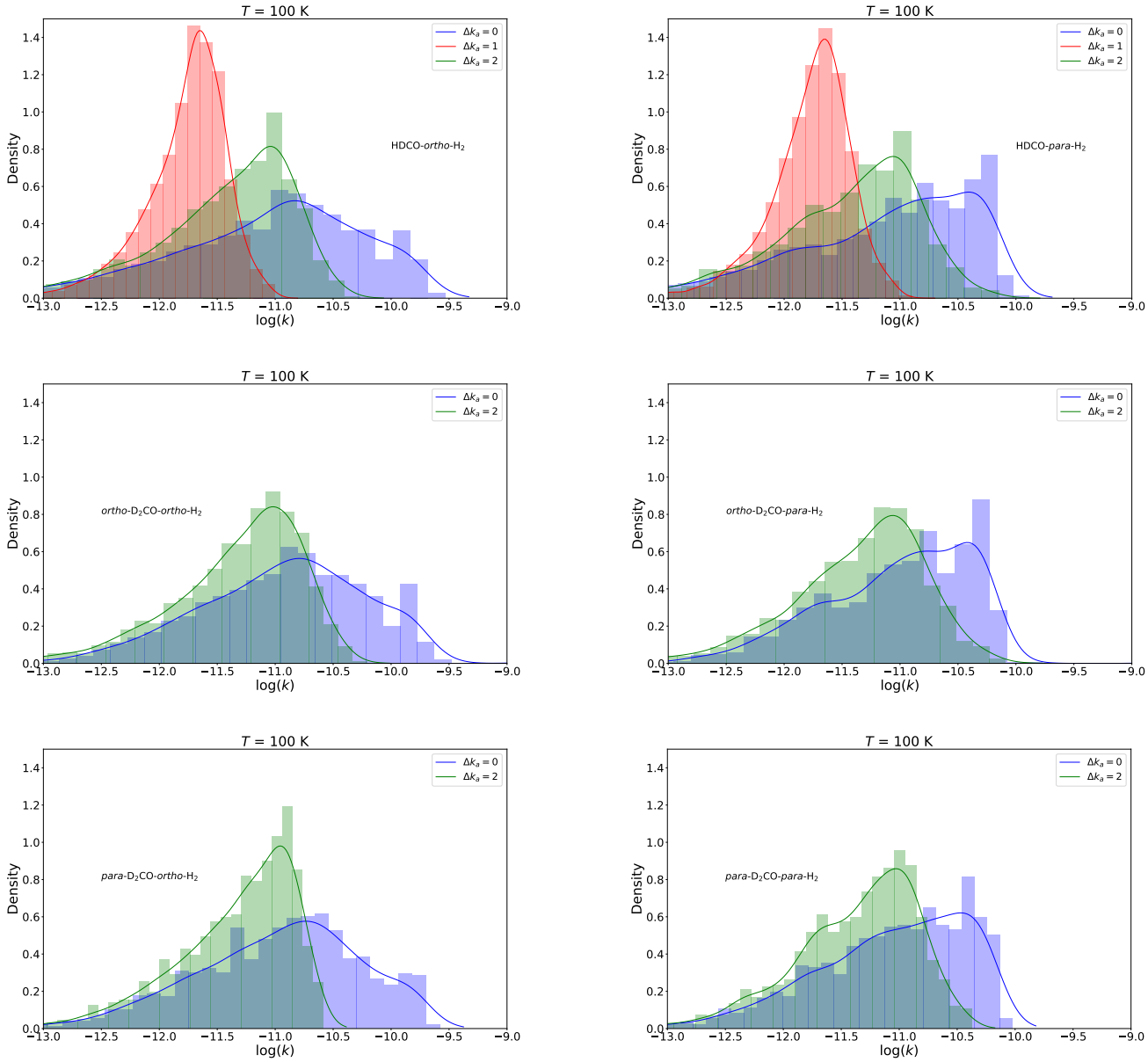


**Fig. 7.** Distribution of the rate coefficient log for HDCO (top), *ortho*-$D_2CO$ (middle), and *para*-$D_2CO$ (bottom) in collision with *ortho*-$H_2$ (left) and *para*-$H_2$ (right) for $T = 100$ K.

broadening coefficients is very good, within 5–17% for the cases of HDCO and $D_2CO$ in collision with *normal*-$H_2$, which is sufficient to validate the accuracy of the PESs and the scattering methodologies employed in this study.

## 4. Excitation of formaldehyde in the ISM

It is interesting to use the computed sets of state-to-state rate coefficients for rotational transitions of formaldehyde isotopologs in collision with *ortho*-$H_2$ and *para*-$H_2$ to investigate their excitation under typical interstellar non-LTE conditions. As an illustrative application, we considered recent detections of the $H_2CO$ ($3_{1,2} \rightarrow 2_{1,1}$), HDCO ($1_{1,1} \rightarrow 0_{0,0}$), and $D_2CO$ ($4_{0,4} \rightarrow 3_{0,3}$) rotational transitions toward the pre-stellar core Corona Australis 151, observed with the Atacama Pathfinder Experiment telescope (Güsten et al. 2006; Redaelli et al. 2025).

We first computed the critical densities ($n^u_{\rm crit}$) of the relevant upper energy levels ($u$) using the formula (McGuire 2022):

$$n^u_{\rm crit}(T) = \frac{\sum_{i<u} A_{ui}}{\sum_{u\neq i} k_{ui}(T)} = \frac{\sum_{i<u} A_{ui}}{\sum_{u\neq i} \left[\frac{\rm OPR}{1+\rm OPR} k^{ortho\text{-}H_2}_{ui}(T) + \frac{1}{1+\rm OPR} k^{para\text{-}H_2}_{ui}(T)\right]}, \quad (16)$$

where OPR is the ortho-to-para ratio of $H_2$ at thermal equilibrium and $A_{ui}$ are the Einstein coefficients for the rotational transitions of $H_2CO$, HDCO, and $D_2CO$ per second. Then, we examined the excitation temperature of the tested lines using non-LTE radiative transfer modeling. Our calculations were performed with the RADEX code, using the escape probability with an expanding sphere (van der Tak et al. 2007). Spectroscopic

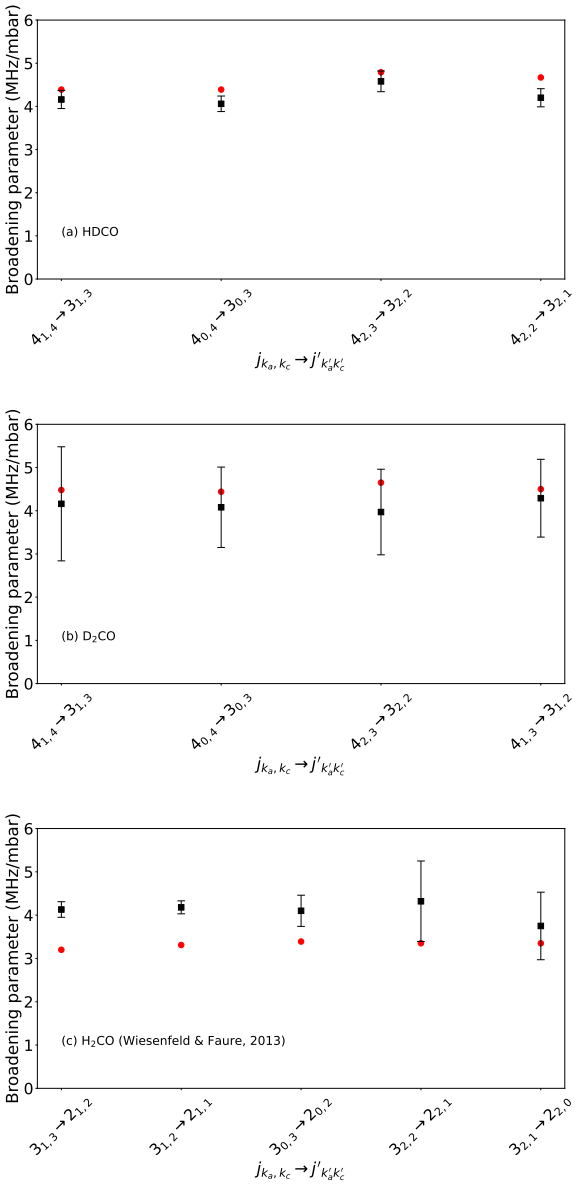


**Fig. 8.** Pressure-broadening parameter (in megahertz per millibar) at 295 K for a set of rotational transitions in (a) HDCO, (b) $D_2CO$ and (c) $H_2CO$ (taken from Wiesenfeld & Faure (2013)). The red circles represent theoretical values, and the black squares with error bars ($3\sigma$) represent experimental measurements.

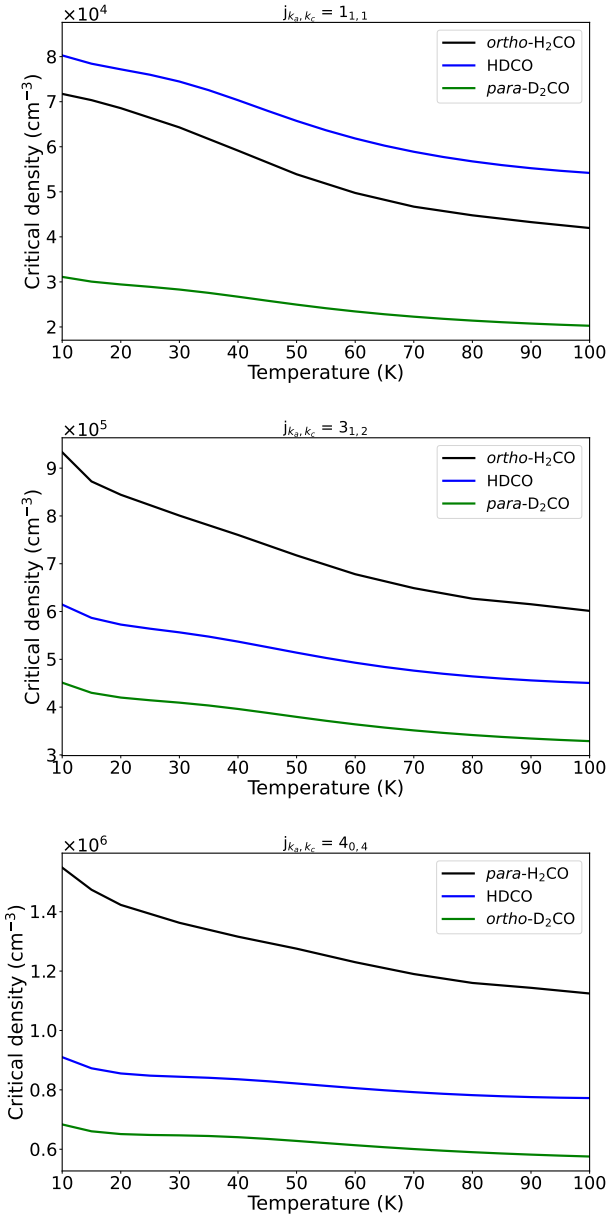


**Fig. 9.** Critical density of several energy levels for the formaldehyde isotopologs as a function of temperature.

data for each isotopolog were taken from the CDMS database (Endres et al. 2016). We assumed a representative line width of $\Delta v = 0.5$ km s$^{-1}$, a column density of $N = 10^{12}$ cm$^{-2}$ for each isotopolog, and a kinetic temperature of $T_{\rm kin} = 10$ K. The cosmic microwave background was adopted as the only external radiation field, with $T_{\rm CMB} = 2.73$ K.

Figure 9 shows the temperature dependence of the critical densities for several rotational energy levels of the three formaldehyde isotopologs. In all cases, the critical densities decrease with increasing temperature, reflecting the increasing contribution of collisions with *ortho*-$H_2$ (at thermal equilibrium). As discussed in Sect. 3, the rate coefficients for the $H_2CO$–$H_2$ system are slightly larger than those for $D_2CO$–$H_2$ and HDCO–$H_2$, despite leading to systematically lower critical densities for $D_2CO$ at a given rotational level. This is due to there being both more open energy levels and lower Einstein coefficients for $D_2CO$ than for $H_2CO$. At the $1_{1,1}$ level, the critical density of HDCO is higher than that of $H_2CO$, as this level corresponds to the lowest *ortho*-$H_2CO$ rotational state and involves fewer radiative decay channels than in the HDCO case. Overall, the critical densities over 10–100 K for the transitions considered here fall in the $10^4$–$10^6$ cm$^{-3}$ range, which is characteristic of dense interstellar cloud conditions.

Figure 10 presents the excitation temperatures ($T_{\rm ex}$) of the selected transitions as a function of the $H_2$ volume density for $T_{\rm kin} = 10$ K. At low densities, $n(H_2) \lesssim 10^2$ cm$^{-3}$; all transitions are thermalized with the background radiation field, with $T_{\rm ex} \simeq T_{\rm CMB}$. As the density increases, the excitation temperatures gradually rise toward LTE, where $T_{\rm ex} = T_{\rm kin}$. This equilibrium is reached at densities above $n(H_2) \gtrsim 10^6 - 10^8$ cm$^{-3}$. The density at which LTE is approached depends strongly on the transition. For instance, the HDCO $1_{1,1} \rightarrow 0_{0,0}$ line approaches

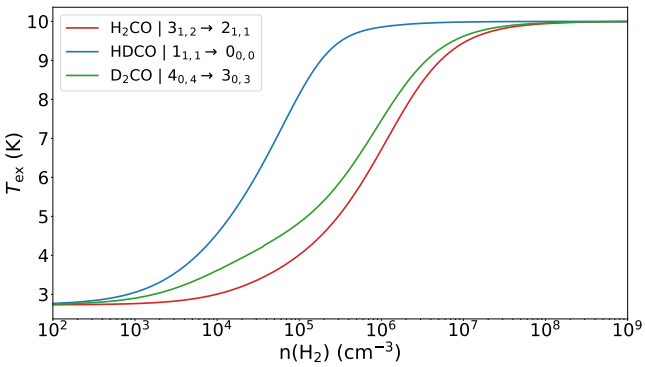


**Fig. 10.** Excitation temperatures for several lines of the formaldehyde isotopologs as a function of the density of $H_2$, for a kinetic temperature of $T_{\rm kin}$ = 10 K.

LTE at densities of a few $10^5$ cm$^{-3}$, while the corresponding transitions of $H_2CO$ and $D_2CO$ remain subthermally excited. This behavior is consistent with the differences in critical densities shown in Fig. 9.

According to Redaelli et al. (2025), the gas density in the Corona Australis 151 pre-stellar core ranges from a few $10^3$ cm$^{-3}$ in the outer regions to a few $10^7$ cm$^{-3}$ at the center. Such pre-stellar cores represent key stages where material is transported from the outer envelope toward the inner regions. Recent high-resolution observations have revealed that material accretion onto protostellar disks often occurs through non-axisymmetric streamers connecting the envelope to the disk (e.g., Yen et al. (2014); Kido et al. (2023)). In this context, tracing the evolution of D/H ratios, particularly through formaldehyde, a key precursor to complex organic molecules, and its deuterated isotopologs such as HDCO and $D_2CO$is crucial for understanding the inheritance of molecular material into planetary systems.

## 5. Conclusion

We reported the first state-to-state collisional rate coefficients for the HDCO–$H_2$ and $D_2CO$–$H_2$ systems. The interaction potentials were derived from the $H_2CO$–$H_2$ PES of Troscompt et al. (2009), transformed to account for isotopic substitution. Time-independent scattering calculations were performed using the CC method to compute cross sections between the 100 lowest rotational states of HDCO and the 60 lowest rotational states of both *ortho*- and *para*-$D_2CO$, in collision with *para*-$H_2$ ($j_2$ = 0) and *ortho*-$H_2$ ($j_2$ = 1). State-to-state rate coefficients were obtained by thermal averaging of the CC cross sections over the collision energy, up to 100 K for the HDCO–$H_2$ and the $D_2CO$–$H_2$ systems.

To extend the temperature range up to 300 K, scattering calculations for collisions involving *ortho*-$H_2$ were performed using the CS approximation, while CC calculations were retained for *para*-$H_2$ collisions using a reduced rotational basis for the projectile. Cross sections and rate coefficients induced by *ortho*-$H_2$ are systematically larger than those induced by *para*-$H_2$, reflecting the enhanced anisotropy of the interaction when $H_2$ is rotationally excited. In addition, HDCO–$H_2$ rate coefficients are generally lower by a factor of 2 to 3 compared to those for $H_2CO$–$H_2$ and $D_2CO$–$H_2$, mainly due to differences in the rotational structure of the energy levels. The break in molecular symmetry for the isotopic substitution in HDCO also resulted in additional transitions lower than those for the two other isotopologs by up to two orders of magnitude. Moreover, rate coefficients for $H_2CO$–$H_2$ are larger than those for $D_2CO$–$H_2$ by up to a factor of 2.

Pressure-broadening coefficients were also computed using the RPA and compared with new laboratory measurements at 295 K. The agreement between theory and experiment is found to be within 30%, providing further validation of the PESs and scattering methodologies used in this work. Finally, the computed collisional data were used in a simple radiative transfer application to illustrate their impact on the excitation of formaldehyde isotopologs under non-LTE conditions typical of cold interstellar clouds.

## Data availability

- Angular expansion coefficients of the HDCO–$H_2$ and $D_2CO$–$H_2$ PESs are provided as a supplementary material for all intermolecular distances as indicated in the file name; all data contain five columns with $l_1$, $m_1$, $l_2$, $l$, expansion coefficients $v_{l_1 m_1 l_2 l}$ (in cm$^{-1}$) (`https://doi.org/10.5281/zenodo.21211294`).
- Collisional rate coefficients for the HDCO–$H_2$ and $D_2CO$–$H_2$ collisional systems produced in this work will be available through the EMAA (Faure et al. 2025) and BASECOL (Dubernet et al. 2024) databases.

*Acknowledgements.* We acknowledge the support from the HOKUSAI BigWaterfall 2 supercomputer within the RB240050 project; the GRICAD infrastructure (https://gricad.univ-grenoble-alpes.fr), which is supported by Grenoble research communities; and the support from the CEA/GENCI (Grand Equipement National de Calcul Intensif) for awarding us access to the TGCC (Très Grand Centre de Calcul) Joliot Curie/IRENE supercomputer. We also thank Lilian Dubray for his work on the early stages of the HDCO–$H_2$ calculations. This study is supported by a Grant-in-Aid from the Ministry of Education, Culture, Sports, Science, and Technology of Japan (JP20H05844, JP20H05845 and JP25H00676) and JSPS Bilateral Program Number JPJSBP120243212 (SAKURA Program between JSPS and MEAE-MESR). AM acknowledges the funding from the European Union's Horizon 2020 research and innovation program under the Marie Skłodowska-Curie grant agreement No 899546 (Ref. BIE22022). This manuscript received the support by RIKEN Special Post Doctoral Reaserchers Program. AM, CSJ and IRS acknowledge financial support from the PHC Sakura program (project number: 51250NB), implemented by the French Ministry for Europe and Foreign Affairs, the French Ministry of Higher Education and Research and the Japan Society for Promotion of Science. CSJ and IRS acknowledge support from the French National Research Agency (ANR) under grant agreement ANR-24-CE30-3044 (project BRIGHTER). IRS thanks the Institut universitaire de France (IUF) and the University of Rennes for travel support. We are grateful to Takuya Hashimoto for helpful discussions and technical guidance on the synthesis of HDCO. We also thank Kohei Tamao for valuable advice on the thermal decomposition process. We acknowledge Genki Kobayashi for providing access to experimental facilities and support, which enabled the successful synthesis of HDCO. We further thank Jean-Claude Guillemin for helpful discussions on the preparation route of deuterated precursors. We thank Satoshi Yamamoto for helpful discussions related to the pressure-broadening measurements. IRS and AF acknowledge financial support from the CNRS MITI interdisciplinary programs through its exploratory research program.

## References

Alexander, M. H. 1984, JCP, 81, 4510
Alexander, M. H. & Manolopoulos, D. E. 1987, JCP, 86, 2044
Babikov, D., Gislason, E. A., Sizun, M., et al. 2002, JCP, 116, 4871
Bacmann, A., Lefloch, B., Ceccarelli, C., et al. 2003, ApJ, 585, L55
Ball, C. D. & De Lucia, F. C. 1998, PRL, 81, 305
Ben Khalifa, M. & Loreau, J. 2024, MNRAS, 527, 846
Caselli, P. & Ceccarelli, C. 2012, AAR, 20
Ceccarelli, C., Caselli, P., Bockelée-Morvan, D., et al. 2014, in Protostars and Planets VI (University of Arizona Press), 944

Ceccarelli, C., Caselli, P., Herbst, E., Tielens, X., & Caux, E. 2007, in Protostars and Planets V, Vol. 951, 47–62
Ceccarelli, C., Codella, C., Balucani, N., et al. 2023, ASPCS, 9, 379
Chahine, L., Ceccarelli, C., De Simone, M., et al. 2024, MNRAS, 534, L48
Dagdigian, P. J. 2022a, MNRAS, 511, 3440
Dagdigian, P. J. 2022b, MNRAS, 514, 2214
Demes, S., Bop, C. T., Ben Khalifa, M., & Lique, F. 2024, PCCP, 26, 16829
Demes, S., Kędziera, D., Faure, A., & Lique, F. 2025, JPCA, 129, 253
Drozdovskaya, M. N., van Dishoeck, E. F., Rubin, M., Jørgensen, J. K., & Altwegg, K. 2019, MNRAS, 490, 50
Dubernet, M. L., Boursier, C., Denis-Alpizar, O., et al. 2024, A&A, 683
Duncan, J. 1974, MP, 28, 1177
Endres, C. P., Schlemmer, S., Schilke, P., Stutzki, J., & Müller, H. S. P. 2016, JMS, 327, 95
Evans, L., Vastel, C., Fontani, F., et al. 2023, A&A, 678
Faure, A., Bacmann, A., & Jacquot, R. 2025, A&A, 700
Faure, A., Szalewicz, K., & Wiesenfeld, L. 2011, JCP, 135, 024301
Faure, A., Valiron, P., Wernli, M., et al. 2005, JCP, 122, 221102
Faure, A., Wiesenfeld, L., Drouin, B., & Tennyson, J. 2013, JQRST, 116, 79
Garrison, B. J., Lester, Jr., W. A., & Schaefer, III, H. F. 1975, JCP, 63, 1449
Green, S. 1991, ApJS, 76, 979
Güsten, R., Nyman, L. A., Schilke, P., et al. 2006, A&A, 454, L13
Hirakawa & Oka. 1956, PPSJ, 1956.7, 25
Huber, K. P. & Herzberg, G. 1979, Molecular Spectra And Molecular Structure, IV. Constants Of Diatomic Molecules (New York: Van Nostrand Reinhold)
Hutson, J. M. & Le Sueur, C. R. 2019, CPC, 241, 9
Jankowski, P. & Szalewicz, K. 2005, JCP, 123, 104301
Johnson, D. R., Lovas, F. J., & Kirchhoff, W. H. 1972, JPCRD, 1, 1011
Joy, C., Bostan, D., Mandal, B., & Babikov, D. 2024, A&A, 692
Kido, M., Takakuwa, S., Saigo, K., et al. 2023, ApJ, 953, 190
Li, S., Sanhueza, P., Lu, X., et al. 2022, ApJ, 939, 102
Linsky, J. L., Draine, B. T., Moos, H. W., et al. 2006, ApJ, 647, 1106
Loinard, L., Castets, A., Ceccarelli, C., et al. 2002, PSS, 50, 1205
McGuire, B. A. 2022, ApJS, 259, 30
McGuire, P. 1975, JCP, 62, 525
Mengel, M. & De Lucia, F. C. 2000, ApJ, 543, 271
Mercimek, S., Codella, C., Podio, L., et al. 2025, MNRAS, 538, 1481
Miettinen, O., Harju, J., Haikala, L. K., & Juvela, M. 2012, A&A, 538
Nomura, H., Furuya, K., Cordiner, M. A., et al. 2022, arXiv2203.10863
Öberg, K. I. 2016, CR, 116, 9631
Okoda, Y., Oya, Y., Sakai, N., Watanabe, Y., & Yamamoto, S. 2020, ApJ, 900, 40
Oyama, T., Ohno, Y., Tamanai, A., et al. 2023, ApJ, 957, 4
Persson, M. V., Jørgensen, J. K., Müller, H. S. P., et al. 2018, A&A, 610
Pirlot Jankowiak, P., Lique, F., & Goicoechea, J. R. 2024, A&A, 683
Podio, L., Ceccarelli, C., Codella, C., et al. 2024, A&A, 688
Pople, J. A., Head-Gordon, M., & Raghavachari, K. 1987, JCP, 87, 5968
Redaelli, E., Spezzano, S., Caselli, P., et al. 2025, A&A, 696
Roueff, E., Parise, B., & Herbst, E. 2007, A&A, 464, 245
Sabatini, G., Podio, L., Codella, C., et al. 2024, A&A, 684
Santelices Rosas, S., Cabrera-González, L. D., Cárdenas, C., & Denis-Apizar, O. 2026, A&A, 708
Schewe, H. C., Ma, Q., Vanhaecke, N., et al. 2015, JCP, 142, 204310
Sogomonyan, K., Ben Khalifa, M., Pierré, P., & Loreau, J. 2025, JCP, 163, 084304
Spezzano, S., Redaelli, E., Caselli, P., et al. 2025, A&A, 694
Tonolo, F. 2025, FASS, 12
Troscompt, N., Faure, A., Wiesenfeld, L., Ceccarelli, C., & Valiron, P. 2009, A&A, 493, 687
Valiron, P., Wernli, M., Faure, A., et al. 2008, JCP, 129, 134306
van der Tak, F. F. S., Black, J. H., Schöier, F. L., Jansen, D. J., & van Dishoeck, E. F. 2007, A&A, 468, 627
Watanabe, Y., Chiba, Y., Sakai, T., et al. 2021, PASJ, 73, 372
Wiesenfeld, L. & Faure, A. 2013, MNRAS, 432, 2573
Wiesenfeld, L., Scribano, Y., & Faure, A. 2011, PCCP, 13, 8230
Yen, H.-W., Takakuwa, S., Ohashi, N., et al. 2014, ApJ, 793, 1
Zakharenko, O., Motiyenko, R. A., Margulès, L., & Huet, T. R. 2015, JMS, 317, 41

## Appendix A: Convergence parameters used in scattering calculations

State-to-state cross sections have been computed using time-independent quantum CC method for collisions between an asymmetric top and a linear rigid rotor using the MOLSCAT code (Hutson & Le Sueur 2019). Coupled equations have been solved using the diabatic modified log-derivative and Airy propagators of Alexander and Manolopoulos (Alexander 1984; Alexander & Manolopoulos 1987). The integration boundaries of the propagator were selected from $R_{\rm min} = 3\ a_0$ to $R_{\rm max} = 100\ a_0$ with a switch between the two propagators at $R_{\rm mid} = 8\ a_0$. Integral cross sections have been converged with respect to the total angular momentum $J_{\rm tot}$ and rotational basis $j_{\rm max}$ up to 1% of accuracy for each selected total energy $E_{\rm tot}$. The $j_{\rm max}$ parameter is also controlled by an energy cutoff $E_{\rm max}$. This last parameter is mostly responsible for the large computational cost. Thus, a convergence of integral cross sections up to 10% with respect to $E_{\rm max}$ was requested. Convergence parameters can be found in Tables A.1–A.2.

## Appendix B: Details on methodologies used in scattering calculations

Although the CC method provides highly accurate scattering results, its computational cost becomes prohibitive at high collision energies. It is therefore necessary to assess the accuracy of approximate treatments and reduced rotational bases, which are known to be system dependent.

For collisions with *para*-$H_2$, tests were first performed at low collision energies using a rotational basis including $j_2 = (0, 2)$, before restricting the basis to $j_2 = 0$ only at higher energies. For both deuterated isotopologs, comparisons between these two bases were carried out at total energies $E_{\rm tot} = 10$, 20, 50, and 100 $\rm cm^{-1}$. Integral cross sections were found to agree within 20–38% of absolute mean error, depending on the collisional system. Similar tests were conducted for collisions with *ortho*-$H_2$, comparing bases including $j_2 = 1$ and $j_2 = (1, 3)$. In this case, differences in the cross section magnitudes were below 7%. This contrast between the two spin modifications arises from the stronger coupling of the $j_2 = 2$ rotational level of $H_2$ to the scattering basis at low energies, compared to the higher $j_2 = 3$ level.

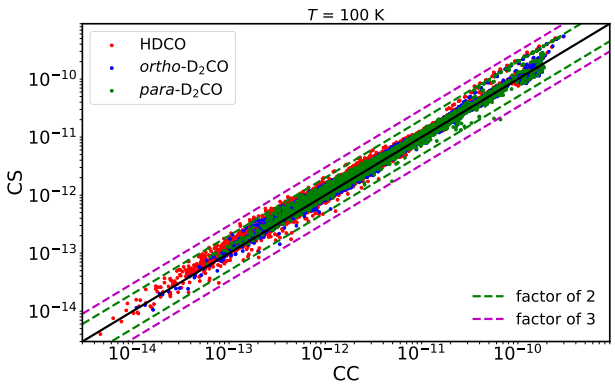


**Fig. B.1.** Systematic comparison of the CC and CS rate coefficients at $T = 100$ K for HDCO and $D_2CO$ when involving collisions with *ortho*-$H_2$.

For collisions involving *ortho*-$H_2$, CC calculations become impractical at high energies, and the CS approximation was therefore employed to extend the calculations. Figure B.1 compares CC and CS rate coefficients at 100 K for all available transitions. For all collisional systems, the two methods agree within a factor of 2 for the majority of transitions, with the CS method slightly overestimating CC results. Fewer than 1% of the data sets deviate by more than a factor of 2 (see Table B.1). Finally, these discrepancies are expected to decrease with increasing temperature, as the CC and CS approaches converge in the high-energy limit.

## Appendix C: Experimental details of pressure-broadening measurements

The pressure-broadening coefficients of $H_2CO$ and its deuterated isotopologs (HDCO and $D_2CO$) were measured using the emission-type millimeter/submillimeter spectrometer SUMIRE (Watanabe et al. 2021). The instrument operates in the frequency range of 211–272 GHz. The absolute intensity accuracy is approximately 6%. In addition, the combination of high spectral resolution and high signal-to-noise ratio ensures that the observed line profiles are reliable. The Doppler line width (HWHM) at room temperature is 0.25–0.30 MHz, which is well resolved with the instrumental resolution (88.5 kHz). The baseline variations occur on a scale much broader than the line width and therefore do not affect the analysis of the line shapes, since it was also minimized by baseline corrections.

At low gas pressures ($\lesssim 0.5$ Pa), the observxed spectral line profiles are dominated by Doppler broadening and can be well reproduced by Gaussian functions. As the pressure increases, collisional effects become significant and the line profiles gradually approach Lorentzian shapes. In this work, molecular hydrogen ($H_2$) was introduced as a buffer gas, and the total gas pressure was varied in order to measure the pressure dependence of the Lorentzian line width. This allowed us to derive the pressure-broadening coefficients (in megahertz per millibar) for collisions with *normal*-$H_2$.

$H_2CO$ and $D_2CO$ were produced by heating commercially available paraformaldehyde (98% purity, FUJIFILM Wako Pure Chemical Corporation) and $d_2$-paraformaldehyde (98 atom% D, Sigma-Aldrich) up to 120°C under vacuum. The generated formaldehyde gas was first introduced into a 500 mL vessel at a pressure of $5.0 \times 10^2$ Pa and subsequently diluted with $H_2$ up to a total pressure of $1.0 \times 10^5$ Pa, yielding a formaldehyde fraction of ~0.5%, thereby preventing repolymerization. The repolymerization was also avoided by conducting the pressure-broadening measurements always within 24h of sample preparation.

HDCO was synthesized via thermal decomposition of partially deuterated calcium formate, following early experimental approaches reported in the literature (Hirakawa & Oka 1956). Calcium hydroxide (96% purity, FUJIFILM Wako Pure Chemical Corporation), formic acid HCOOH (99% purity, FUJIFILM Wako Pure Chemical Corporation), and deuterated formic acid DCOOH (chemical purity of 95% and isotopic purity of 98 atom% D) were mixed in equimolar proportions. A mixture of $H_2O$ and $D_2O$ was added to facilitate homogenization, and the solution was stirred. The mixture was then heated to 150°C to remove water, yielding a solid powder of partially deuterated calcium formate, Ca(HCOO)(DCOO). The obtained sample was further dried under vacuum at 120°C and subsequently heated up to 450°C to induce thermal decomposition, producing a gas mixture. The resulting gas contains $H_2CO$, $D_2CO$, HDCO, and CO as the main detectable species. Their relative abundances were estimated from the observed rotational line in-

**Table A.1.** Convergence parameters for the HDCO–$H_2$ collisional system.

| HDCO–*para*-$H_2$ | | | | | HDCO–*ortho*-$H_2$ | | | | |
|---|---|---|---|---|---|---|---|---|---|
| $E_{tot}$ | $\Delta E_{tot}$ | $j_{max}$ | $E_{max}$ | $J_{tot}$ | $E_{tot}$ | $\Delta E_{tot}$ | $j_{max}$ | $E_{max}$ | $J_{tot}$ |
| 10 | 0.1 | 14 | 500 | 10 | 128.7 | 0.1 | 16 | 300 | 23 |
| 20 | 0.1 | 14 | 550 | 13 | 138.7 | 0.1 | 16 | 300 | 29 |
| 50 | 0.1 | 15 | 550 | 19 | 168.7 | 0.1 | 16 | 300 | 33 |
| 60 | 0.1 | 15 | 550 | 20 | 178.7 | 0.1 | 18 | 350 | 35 |
| 75 | 0.2 | 17 | 550 | 22 | 193.7 | 0.2 | 18 | 350 | 36 |
| 100 | 0.2 | 18 | 550 | 25 | 218.7 | 0.2 | 19 | 400 | 41 |
| 150 | 0.5 | 19 | 600 | 29 | 268.7 | 0.5 | 20 | 400 | 47 |
| 200 | 0.5 | 22 | 600 | 32 | 318.7 | 0.5 | 22 | 450 | 50 |
| 300[a] | 10 | 22 | 600 | 37 | 418.7 | 10 | 23 | 500 | 52 |
| 400 | 10 | 24 | 650 | 41 | 518.7[b] | 10 | 23 | 550 | 56 |
| 500 | 50 | 24 | 850 | 45 | 618.7 | 50 | 23 | 850 | 62 |
| 600 | 50 | 25 | 900 | 49 | 718.7 | 50 | 23 | 850 | 65 |
| 700 | 50 | 25 | 1050 | 52 | 818.7 | 50 | 24 | 1000 | 67 |
| 800 | 50 | 27 | 1100 | 54 | 918.7 | 50 | 25 | 1050 | 69 |
| 900 | 50 | 27 | 1100 | 57 | 1018.7 | 50 | 26 | 1100 | 70 |
| 1000 | 100 | 28 | 1100 | 59 | 1118.7 | 100 | 26 | 1150 | 72 |
| 1100 | 100 | 30 | 1100 | 61 | 1218.7 | 100 | 28 | 1200 | 74 |

**Notes.** [a] Switch to CC calculations with $j_{2,max} = 0$. [b] Switch to CS calculations.

tensities measured with the SUMIRE spectrometer. The intensity calibration of the instrument has previously been independently validated through laboratory measurements of transition line strengths (Oyama et al. 2023). The resulting abundances of $H_2CO$, $D_2CO$, HDCO, and CO were estimated to be approximately 4%, 3%, 9%, and ∼26% respectively. Additional gas components such as $H_2$ and $CO_2$ are also expected to be present but do not contribute to rotational transitions due to their lack of a permanent electric dipole moment. The gas mixture was introduced into the 500 mL vessel at $1.5 \times 10^3$ Pa and further diluted with $H_2$ up to $2.7 \times 10^4$ Pa. Under these conditions, the effective abundance of HDCO relative to $H_2$ was at most ∼0.5%, and the abundance of impurities was limited to a few percent. Therefore, self-collision effects can considered to be negligible.

The prepared gas mixture was then transferred to the 2 m glass cell of the SUMIRE spectrometer. The gas was introduced at an initial pressure of ∼5 Pa, and additional $H_2$ was added to vary the total pressure between 5.1 and 41 Pa. Rotational spectra were then measured at room temperature at several discrete pressure points. Representative spectra at selected pressures are shown in Fig. C.1.

The observed spectral lines were analyzed using Voigt profile fitting, and the pressure-broadening coefficient was then derived as the slope of the Lorentzian line width (HWHM) as a function of pressure. The Doppler width (HWHM) was fixed to the theoretical value (0.25–0.30 MHz) at room temperature for each molecule and transition. In each transition, the Lorentzian line width shows a clear linear dependence on pressure, as can be observed in Fig. C.2.

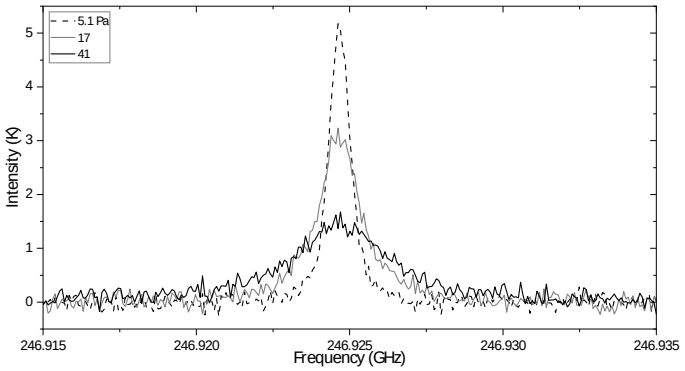


**Fig. C.1.** Representative observed spectral lines at selected pressures (5.1, 17, and 41 Pa), overplotted, for the $4_{1,4} \rightarrow 3_{1,3}$ transition of the HDCO molecule. The evolution of the line shape reflects the transition from Doppler to collisional broadening with the $H_2$ collider.

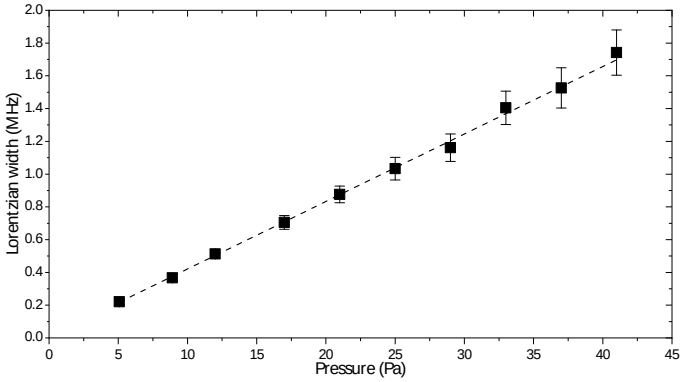


**Fig. C.2.** Linear regression analysis of the Lorentzian line width as a function of the pressure for the $4_{1,4} \rightarrow 3_{1,3}$ transition of HDCO. The Doppler width is fixed at the theoretical value of 0.27 MHz at room temperature. The uncertainty of $3\sigma$ is shown.

**Table A.2.** Convergence parameters for the $D_2CO$–$H_2$ collisional system.

| *para*-$D_2CO$–*para*-$H_2$ | | | | | *para*-$D_2CO$–*ortho*-$H_2$ | | | | |
|---|---|---|---|---|---|---|---|---|---|
| $E_{tot}$ | $\Delta E_{tot}$ | $j_{max}$ | $E_{max}$ | $J_{tot}$ | $E_{tot}$ | $\Delta E_{tot}$ | $j_{max}$ | $E_{max}$ | $J_{tot}$ |
| 16.6 | 0.1 | 16 | 450 | 11 | 134.3 | 0.1 | 13 | 350 | 25 |
| 26.6 | 0.1 | 16 | 450 | 15 | 144.3 | 0.1 | 14 | 350 | 33 |
| 56.6 | 0.1 | 19 | 500 | 20 | 174.3 | 0.1 | 18 | 350 | 45 |
| 66.6 | 0.1 | 20 | 500 | 21 | 184.3 | 0.1 | 18 | 350 | 48 |
| 81.6 | 0.2 | 20 | 500 | 24 | 199.3 | 0.2 | 19 | 400 | 51 |
| 106.6 | 0.2 | 24 | 650 | 27 | 224.3 | 0.2 | 20 | 450 | 54 |
| 156.6 | 0.5 | 25 | 650 | 30 | 274.3 | 0.5 | 20 | 450 | 56 |
| 206.6 | 0.5 | 26 | 650 | 34 | 324.3 | 0.5 | 21 | 650 | 58 |
| 306.6[a] | 10 | 26 | 750 | 40 | 424.3 | 10 | 22 | 650 | 65 |
| 406.6 | 10 | 26 | 800 | 44 | 524.3 | 10 | 23 | 650 | 67 |
| 506.6 | 50 | 27 | 800 | 49 | 624.3[b] | 50 | 25 | 650 | 71 |
| 606.6 | 50 | 27 | 900 | 52 | 724.3 | 50 | 26 | 850 | 72 |
| 706.6 | 50 | 27 | 900 | 55 | 824.3 | 50 | 26 | 900 | 73 |
| 806.6 | 50 | 28 | 1000 | 57 | 924.3 | 50 | 26 | 950 | 75 |
| 906.6 | 50 | 28 | 1100 | 60 | 1024.3 | 50 | 27 | 1000 | 78 |
| 1006.6 | 100 | 29 | 1200 | 65 | 1124.3 | 100 | 27 | 1100 | 79 |
| 1106.6 | 100 | 31 | 1200 | 66 | 1224.3 | 100 | 28 | 1200 | 81 |
| *ortho*-$D_2CO$–*para*-$H_2$ | | | | | *ortho*-$D_2CO$–*ortho*-$H_2$ | | | | |
| $E_{tot}$ | $\Delta E_{tot}$ | $j_{max}$ | $E_{max}$ | $J_{tot}$ | $E_{tot}$ | $\Delta E_{tot}$ | $j_{max}$ | $E_{max}$ | $J_{tot}$ |
| 10 | 0.1 | 16 | 450 | 14 | 128.7 | 0.1 | 14 | 350 | 26 |
| 20 | 0.1 | 16 | 500 | 15 | 138.7 | 0.1 | 15 | 350 | 33 |
| 50 | 0.1 | 17 | 550 | 20 | 168.7 | 0.1 | 16 | 350 | 38 |
| 60 | 0.1 | 17 | 550 | 24 | 178.7 | 0.1 | 16 | 350 | 45 |
| 75 | 0.2 | 18 | 550 | 25 | 193.7 | 0.2 | 17 | 350 | 50 |
| 100 | 0.2 | 20 | 550 | 26 | 218.7 | 0.2 | 17 | 350 | 54 |
| 150 | 0.5 | 22 | 700 | 31 | 268.7 | 0.5 | 19 | 500 | 59 |
| 200 | 0.5 | 22 | 750 | 36 | 318.7 | 0.5 | 21 | 600 | 62 |
| 300 | 10 | 25 | 750 | 42 | 418.7 | 10 | 23 | 600 | 67 |
| 400[a] | 10 | 25 | 750 | 45 | 518.7 | 10 | 24 | 600 | 70 |
| 500 | 50 | 26 | 900 | 48 | 618.7 | 50 | 24 | 650 | 74 |
| 600 | 50 | 27 | 950 | 55 | 718.7[b] | 50 | 26 | 800 | 75 |
| 700 | 50 | 27 | 950 | 57 | 818.7 | 50 | 27 | 900 | 77 |
| 800 | 50 | 28 | 950 | 58 | 918.7 | 50 | 27 | 950 | 78 |
| 900 | 50 | 30 | 950 | 60 | 1018.7 | 50 | 27 | 1000 | 80 |
| 1000 | 100 | 32 | 1100 | 63 | 1118.7 | 100 | 28 | 1100 | 81 |
| 1100 | 100 | 33 | 1100 | 65 | 1218.7 | 100 | 29 | 1200 | 82 |

**Notes.** [(a)] Switch to CC calculations with $j_{2,max} = 0$. [(b)] Switch to CS calculations.

**Table B.1.** Number of transitions for several ratio of deviations between CC and CS methods at 100 K for HDCO and $D_2CO$, both in collision with *ortho*-$H_2$.

| $\max(k_{CC}/k_{CS}, k_{CS}/k_{CC})$ | HDCO | *ortho*-$D_2CO$ | *para*-$D_2CO$ |
|---|---|---|---|
| $> 2$ | 64 | 11 | 13 |
| $< 2$ | 9898 | 3536 | 3420 |